Study of Evaporation Residues of
the Reaction $^{48}Ca + {}^{176}Yb$

By Jeremy P. Seitz

A THESIS

Submitted to
Michigan State University
in partial fulfillment of the requirements
for the degree of

MASTER OF SCIENCE

Department of Physics and Astronomy

2003

ABSTRACT

Study of Evaporation Residues of the Reaction $^{48}Ca + ^{176}Yb$

By

Jeremy P. Seitz

Giant dipole resonances have long been studied to probe the dynamics of fusion reactions. Until now, the GDR from such a heavy fusion reaction has not been measured in coincidence with the evaporation residue. Using the reaction ^{48}Ca on ^{176}Yb we measured the GDR in highly excited ^{224}Th. Such ER coincidence measurements make possible the use of the GDR to better probe such highly fissile systems.

Previous evidence by Brinkman *et. al.* had indicated an excess cross section at high excitation energies from $^{16}O+^{208}Pb$. Our ability to study the cross section, angular momentum distribution and GDR from ^{48}Ca on ^{176}Yb provided an excellent opportunity to probe this effect further. The observed cross section did not exhibit the excess previously observed, supporting Berriman's *et. al.* assertion that the excess cross section is from incomplete fusion. However, the angular momentum distribution did indicate possible fission hindrance.

The experiment was performed at Argonne National Laboratory with a beam of 206 MeV, 219 MeV and 259 MeV ^{48}Ca. A 150 crystal BaF_2 array was used for high energy γ-ray detection. A 48 crystal BGO array was used for multiplicity measurements and the Fragment Mass Analyzer provided particle identification.

Contents

List of Figures

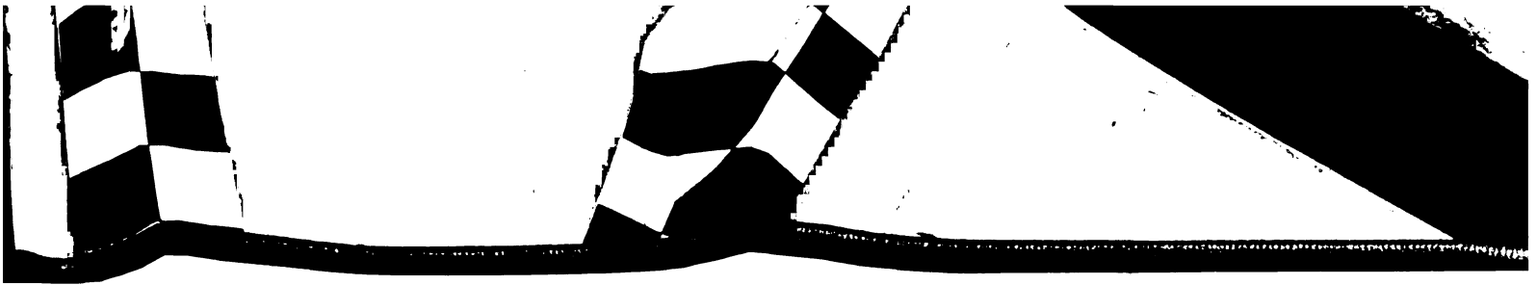

List of Tables

Chapter 1

Introduction

The Giant Dipole Resonance (GDR) built on highly excited states has been used extensively to study nuclear structure at finite temperatures and angular momentum. More recently it has been used to study the characteristics of fusion fission reactions.

Recent studies show an excess of high-energy (pre-fission) γ-rays. This supports the prior findings that fission in hot nuclei is slower than predicted by standard statistical models and perhaps partially inhibited.

The timing of the excess GDR γ-ray emissions has important implications. If the γ-rays are emitted prior to the saddle point, the emission could change the dynamics of the compound nucleus cascade. This change could manifest itself in several ways; an overall change in evaporation residue (ER) cross section, a shift of the final ER mass distribution or possibly a change in the final angular momentum distribution. However, if the excess γ-rays are emitted after the saddle point, there should be no affect on the mass distribution, cross section or angular momentum distribution.

The composition of the mass distribution is one measure of the initial angular momentum distribution. During the cascade, high angular momentum compound nuclei (CN) will have a high propensity to α-decay, reducing the average mass of the ER. However, if the excess emissions are from before the saddle, more high angular

momentum CNs would survive the saddle, thus changing both the mass distribution and the angular momentum distribution of the CNs that cascade.

1.1 Giant Dipole Resonance

Modern nuclear physics is based on the use of observables to probe the structure of the nucleus. Nuclear structure's nature prevents a direct analysis of its properties and characteristics. To overcome this obstacle, physicists have developed and discovered many methods of indirect analysis. The most notorious of examples is the gold-foil experiment by Rutherford in 1911 [4]. His analysis of nucleus-scattered alpha particles gave the first profound insight into the structure of the atom. The methods today have not changed significantly, though the analysis has become increasingly sophisticated. The new coupled cyclotron at the National Superconducting Cyclotron Laboratory can bombard targets with rare radioactive isotopes while almost all reaction products can be separated and collected with tools such as the S800 mass spectrometer and 4π detector arrays.

Nuclear excitation is one of the new tools employed by physicists to gain insight into the structure of the nucleus. The nature of the excitation can be analyzed like the sound from a bell in a 'black box.' The ring of the bell gives you profound insight, even without direct observation of the bell. So too do the symptoms of excitation give you insight into the characteristics of the nucleus.

There are two types of excitation that occurs within the nucleus, single particle and collective [5]. Single particle excitation is the movement of single nucleons between energy states in the nucleus [6]. These interactions have been successfully described by microscopic models of the nucleus. However, collective excitation is not easily described by microscopic models and only general factors can be described by macroscopic models. The characteristics of surface tension, collective motion, rota-

tion and vibration have all been modeled in this way.

Giant resonances are collective vibration of the nucleons. This collective excitation has several multipolarities; monopole, dipole, quadrupole and so on. The monopole resonance, often referred to as the 'breathing' mode, is effectively the deflation and inflation of the nucleus (see figure 1.1). This mode is excited by elastic scattering, and characterized by a diffraction pattern formed by scattered wavelets. The second mode, dipole resonance, is characterized by absorption (or emission) of resonance energy γ-rays. The dipole resonance is the easiest to study and was originally induced through mono-energetic photon E-field interaction. The picture that is commonly applied to the dipole mode is that of the proton's collective motion from side to side with stationary neutrons. This motion results from the interaction of the protons with the experimenter's projectile and the lack of neutron interaction. Quadrapole vibrations are induced primarily by proton or alpha inelastic scattering and characterized by diffraction patterns. Higher order vibrations have only recently been observed and quickly become swamped by other effects.

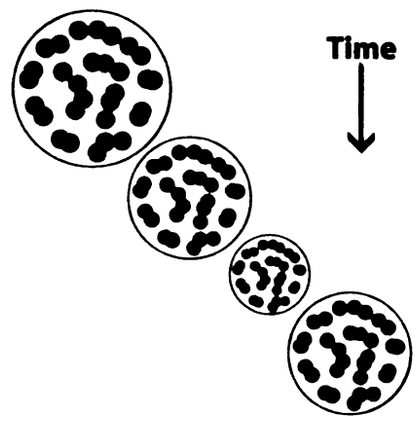

Figure 1.1: Illustration of the monopole or 'breathing' mode of giant resonance.

A very early classical model of dipole resonance is attributed to Russian physicist

Arkadii Migdal [7]. With this model of the nucleus, one can easily predict the dipole frequency from

$$\omega^2 \propto F_{restore}/I_{inertia}. \tag{1.1}$$

The restoring force can be modeled in different ways, but is normally some measure of the strong force (binding energy) and the inertia (merely the mass of the nucleus). Though this is a fairly naive model, predicted values of the dipole match fairly well. The modern, more sophisticated model used to predict vibrations in the nucleus is the liquid drop model (LDM). This model is a combination of the Goldhaber-Teller (GT) and Steinwedel-Jensen (SJ) model [7]. Both based on liquid drop oscillations, they take slightly different approaches. The GT method treats the neutrons and protons as independent incompressible liquids. As they oscillate out of phase, the two spheres effectively separate, overlap and separate on the opposite side (see figure 1.2.a). This approach leads to

$$\omega^2 \propto F_{restore} \propto A^{-2/3} \tag{1.2}$$

The SJ method views the nucleus as bounded by a hard shell which maintains its shape. The nucleon density then shifts within the shell. The oscillation would consist of an increased proton density on one side with neutrons on the other, and then opposite (figure 1.2.b). This model leads to

$$\omega^2 \propto F_{restore}/R^3 \propto A^{-1/3} \tag{1.3}$$

However, neither model easily predicted resonances for different masses. Instead, a mixture of the two models is used to accurately predict the energy.

$$E_{GDR} = 31.2A^{-1/3} + 20.6A^{-1/6}[MeV] \tag{1.4}$$

Giant resonances have been studied in depth for many years [8] in order to gain understanding of the internal forces of the nucleus. Extracting the sensitivities of giant resonance parameters allows more rigorous testing of nuclear models such as those by Migdel and Bohr. Though a great deal of study has been completed on the characteristics of GDR, several questions remain unanswered. The study of GDR in highly excited nuclei has further pushed the models, but temperature and angular momentum dependence of the GDR width has never been well determined.

1.1.1 GDR Built on Excited States

When the nucleus is in an excited state and exhibits collective oscillation it is said to have giant resonances (GR) built on the excited state. First suggested in 1955 by David Brink, the phenomenon of GDR built on excited states is a natural extension of the ground state oscillation [7].

The coupling of the GDR energy to the nucleus' radius (as seen in equation 1.4) means the GDR is sensitive to nuclear deformation. The energy splitting of the GDR that is seen gives important insight into shape fluctuations and reaction mechanics.

The two shape fluctuations associated with GDR are prolate and oblate oscillations. The prolate oscillation is pictured by a football shape with two short and one long axis. The short axis, corresponding to the higher energy, can have a GDR γ-ray

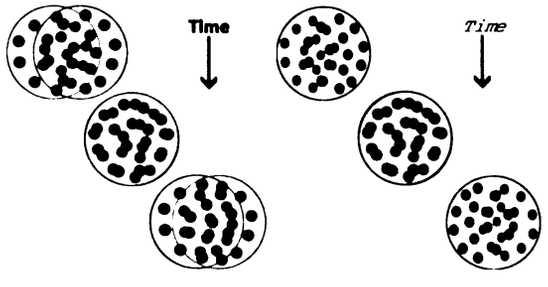

Figure 1.2: Giant dipole resonance. a: (left) GT model of GDR. b: (Right) ST description of GDR.

strength of up to twice that of the long axis (corresponding to superdeformation). The oblate shape is that of a pancake, leading to more long-axis, low energy γ-rays than short, high energy emissions.

The emission of γ-rays which are used to measure the GDR are in competition with the evaporation processes and fission. The GDR γ-rays are then coming from multiple phases of the excitation and de-excitation process. This has lead to both experimental challenges as well as opportunities to analyze the time dependence of the experiment. Particular interest has been shown in using the GDR as a fission clock to analyze the dynamics of the reaction [8]. Prefission γ-ray strength and evaporation cross section are important observables used to extract fission timescales and dynamics. The increased cross section of evaporation residues in some experiments [8] have not previously been reconciled. Those unexplained data beg further study of the sensitive observables in similar reactions.

1.2 Angular Momentum Distribution of Evaporation Residue

The cascade from reaction product to evaporation residue follows a distinct path in all fusion evaporation reactions (figure 1.3). The reaction product starts with a certain excitation energy, some of which is tied up in angular momentum. In reactions such as ^{48}Ca on ^{176}Yb at 250 MeV, a vast majority of the products immediately fission due to the smaller fission barrier at large angular momentum. The remaining products cascade down to the yrast line by E1-γ-rays, and particle emission. Once on the yrast line, the ER will evaporate low-energy E2-γ rays until it reaches the ground state.

An analysis of the angular momentum distribution for the reaction should provide important details about the mechanics of fusion-fission reactions. Mapping of the

angular momentum distribution in coincidence with the evaporation residues allow us to make comparisons with statistical models and look for abnormalities. If the angular momentum distribution is deficient in a specific region, it could be an indication of pre-saddle hindrance leading to fission [9]. A simulation that illustrates this was done by Thoennessen et al. with the statistical model CASCADE and is shown in figure 1.4.

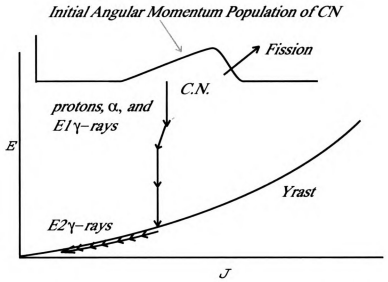

Figure 1.3: Typical decay of a fusion evaporation reaction. Angular momentum (J or k) is directly proportional to multiplicity (2:1 multiplicity to angular momentum ratio). The Yrast line denotes the minimum excitation energy to support the corresponding angular momentum.

1.3 The Reaction

We chose the neutron deficient ^{224}Th for our studies because it is the most completely explored nucleus for this type of analysis. Fission and evaporation residue cross section as well as pre-fission neutron, charged particles and γ-ray measurements have been performed. In addition, there were indications in the reaction ^{16}O+^{208}Pb that

a reasonably large evaporation residue cross section remains even at high excitation energies. This ER excess is not predicted in standard statistical calculations.

Using the reaction ^{48}Ca on ^{176}Yb to study highly excited ^{224}Th, we measured the GDR strength function and angular momentum distribution in coincidence with evaporation residues. The first phase of the experiment, measurement of the cross section and angular momentum distribution, was completed with 259 MeV, 219 MeV and 206 MeV ^{48}Ca beam. The second part of the experiment was done with a 256 MeV Ca beam to produce ^{224}Th with an excitation energy of 80 MeV.

Unlike neutron experiments, it is not possible to distinguish between γ-rays emitted by the compound system and the fission fragments. In order to measure a clean GDR spectrum of the highly fissile system, it was necessary to use γ-rays in coincidence with ER.

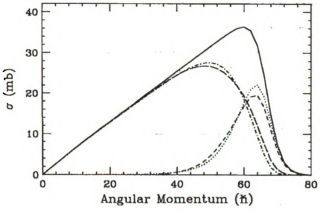

Figure 1.4: Sample calculated angular momentum distributions showing the enhancement of the high angular momentum region when pre-saddle fission hindrance is included. Total fusion (solid). Evaporation residue (dot-dash). Fission (dotted). With dissipation: ER (long-dashed), fission (short-dashed). Figure reprinted from [1]

Chapter 2

Experimental Setup

The experiment was performed at Argonne National Laboratory (ANL) with the ANL Tandem Linac Accelerator System (ATLAS). The setup consisted of the Michigan State University (MSU), Oak Ridge National Lab and Texas A&M University 150 crystal BaF_2 array, 40 crystal ANL BGO array and the ANL Fragment Mass Analyzer(FMA). A picture of the setup can be seen in figure 2.1

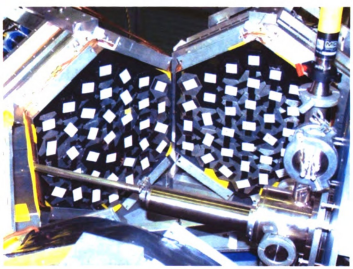

Figure 2.1: Picture of the target chamber. The beam enters from the left and enters the FMA (not shown) on the right. The BaF_2 packs can be seen surrounding the target chamber.

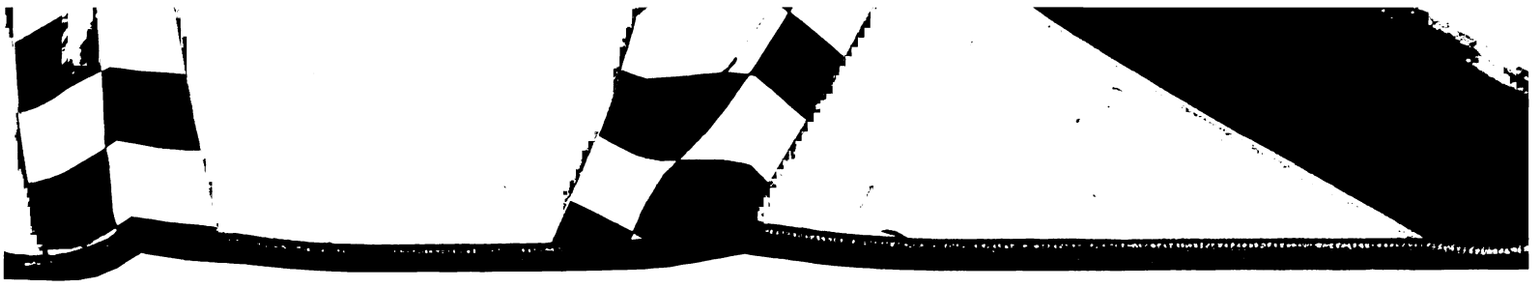

The experiment ran with two different configurations, first with the BGO array close to the reaction chamber and next with the BGO pulled out. The first configuration required the BGOs packed closely around the target, thereby shadowing a portion of the BaF_2. In this position the BGO was a very effective multiplicity filter. The BGO was moved out for the second portion of the experiment to allow for maximum efficiency of the BaF_2. In this configuration, the BGO's function as a multiplicity filter turned out to be significantly impaired. However, the BaF_2 could then be used to collect a high resolution γ-ray spectrum of the highest energy beam (259 MeV).

2.1 Target Chamber

The target chamber was fabricated to allow the maximum closure of the BGO and BaF_2 packs without beam-loss due to pipe walls. To maximize beam time, the target was mounted on a rotating arm so the chamber would not need to be opened during experiments. The target wheel contained an empty target (for focusing), a Ni target ($663\mu g/cm^2$) for calibration, and two Yb targets ($810\mu g/cm^2$) for the principle reaction. To accomplish all of this, the beam-pipe was 1 inch in diameter up to the target and 2.5 inches between the target and FMA. The target chamber was wrapped in three foils to minimize low energy x-rays and reduce the overall count-rate in the BaF_2 detectors. The foils were 10 mil Ta, Cd, Cu. The chamber itself was 1/16 inch aluminum.

The target used during the experiment was ^{176}Yb with a thickness of $810\mu g/cm^2$. The beam-spot was wobbled throughout the experiment to reduce the beam intensity on the target. The wobble allowed higher beam intensity without damage to the target. The wobble was produced by oscillating the steering magnets just upstream of the setup. This was done without significant loss of FMA resolution [10].

2.2 BaF_2 Array

The BaF_2 Array is a collection of detectors from Oak Ridge National Laboratory, Texas A&M University and Michigan State University. The coupling grease between the phototube and crystal degrades over time, affecting the resolution. The detectors were reconditioned shortly before the experimental array was assembled to minimize this effect.

The BaF_2 crystals were set up in four packs of 37 crystals each. Each pack was a hexagon that was perfectly filled with the crystals, leaving only a 1/8 inch gap between crystals (due to the wrapping material). The frame was an aluminum cage mounted horizontally with the center of the pack pointed toward the target as shown in figure 2.2. Two of the packs were at 90° with the target, and two were located at 121° (upstream). The face of the packs were 15.5 inches from the target for both packs.

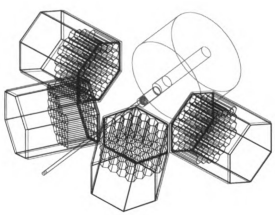

Figure 2.2: BaF_2 packs (left), FMA (right) target chamber (center). The beam enters from the bottom left.

2.2.1 Efficiency and Resolution

The resolution of the individual BaF_2 detectors were increased significantly during the reconditioning. There was a 2-4% increase in resolution, to an average of 14%. The detectors ranged from 10-20% though few were over 16%. Detectors were arranged in the packs to maximize the use of high resolution detectors.

The array resolution was affected by the drift of the individual detectors. An approximate gain calibration was done online automatically. However, off-line gain calibration was still needed. ^{88}Y was used to calibrate the detectors twice a day. This data, combined with high-energy proton and PuC runs, were used to create a time-dependent calibration for each detector. A sample of the correction can be seen in figure 2.4. The crystals temperatures were also recorded, but found to have no appreciable effect on the calibration.

2.2.2 Shower Reconstruction

To enhance the energy and multiplicity resolution of the BaF_2 packs, shower reconstruction was performed off-line. The reconstruction is a technique of identifying different showers in the pack and summing the energy of the detectors hit by a shower. A nearest neighbor technique was used to identify signals most likely to be associated with a particular shower. The maximum showers per block was three. Any more tended to lead to cross-shower confusion.

Figure 2.3: A BaF_2 pack with 48 detectors stacked inside.

Shower reconstruction was obviously most effective in the high energy region, where it was needed most. The effect of reconstruction can be seen in figure 2.5.

2.3 BGO Array

The Argonne-Notre Dame BGO array consists of 50 hexagonal BGO detectors. The detectors were used as a multiplicity filter for the reaction at 106, 119 and 259 MeV. For these measurement, the array was fully closed around the target chamber as seen in figure 2.6. The shadowing of the BaF_2 that this caused was significant, however, the BaF_2 array was not important for the angular momentum distribution measurement. The BGO array was run with a multiplicity greater than one requirement to reduce dead-time.

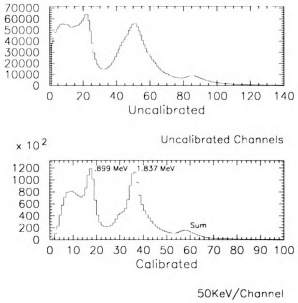

Figure 2.4: Sample of the increased resolution with a time-dependent offline calibration of the BaF_2.

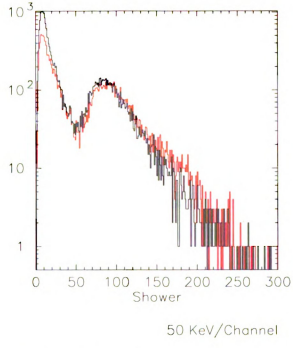

Figure 2.5: Effect of the shower reconstruction. Note the reconstructed spectrum (red) has enhanced features at high energy.

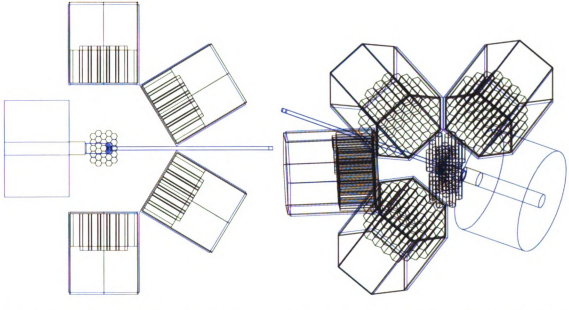

Figure 2.6: Experimental setup with the BGOs 'closed' around the target chamber. The BaF_2 array and FMA can also be seen.

2.4 Fragment Mass Analyzer

The trigger for both portions of the experiment included evaporation residue in the FMA. The FMA was used to separate the reaction products by mass divided by charge (M/q). The acceptance of the FMA was 11 degrees for the experimental setup. The acceptance allowed for fast neutron and alpha emissions from the ER. The 11° opening of the FMA allowed for 90° 1 MeV neutron emitters, and 25 MeV alpha emitters. The alpha and neutron emissions were predicted to be well below the acceptance energies. The overall efficiency of the FMA is approximately 15%, without taking into account the lifetime or mass acceptance of the residues.

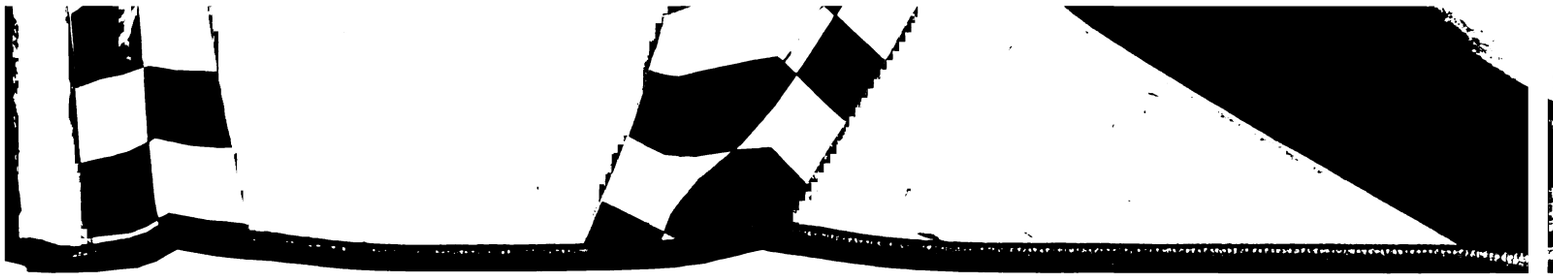

Chapter 3

Data Analysis

3.1 Mass Identification with the FMA

3.1.1 Calibration with Ni

A preliminary calibration of the FMA was done using a ^{48}Ca beam on a Ni target. The observed mass spectrum (figure 3.1) was compared to the results from the FMA M/q calculator [11]. The calculation was run with a gain calibrated to the apparent mass separation from the experimental plot. The gain was found by matching the predicted mass separation and the observed mass separation. The observed mass separation was approximately 29 channels/mass for nickel and lead to a FMA gain setting of 2700. Table 3.1 shows a comparison of those values. This comparison reveals a good agreement between the predicted and observed values.

3.1.2 Absolute Cross Section

The absolute cross section of the ER was found for all three energies (see table 3.2). These values were calculated from the integrated charge of the beam (IQ), raw ER counts (Y) and runtime (t). A sample calculation can be seen here.

Chapter 3

Data Analysis

3.1 Mass identification with the EMA

3.1.1 Calibration with Ni

A preliminary calibration of the EMA was done using a ^{58}Ca beam on a Ni target. The observed mass spectrum (figure 3.1) was compared to the results from the PMA M/q calculator [1]. The calculation was run with a gain calibrated to the approximate mass separation from the experimental data. The gain was found by matching the predicted mass separation and the observed mass separation. The observed mass separation was approximately 20 channels/mass for ridged and 1ed to a EMA gain setting of 2700. Table 3.1 shows a comparison of these values. This comparison reveals a good agreement between the predicted and observed values.

3.1.2 Absolute Cross Section

The absolute cross section of the BF was found for all three energies (see table 3.2). These values were calculated from the integrated charge of the beam ($\int Q$), raw BF counts (Y) and runtime (t). A sample calculation can be seen here:

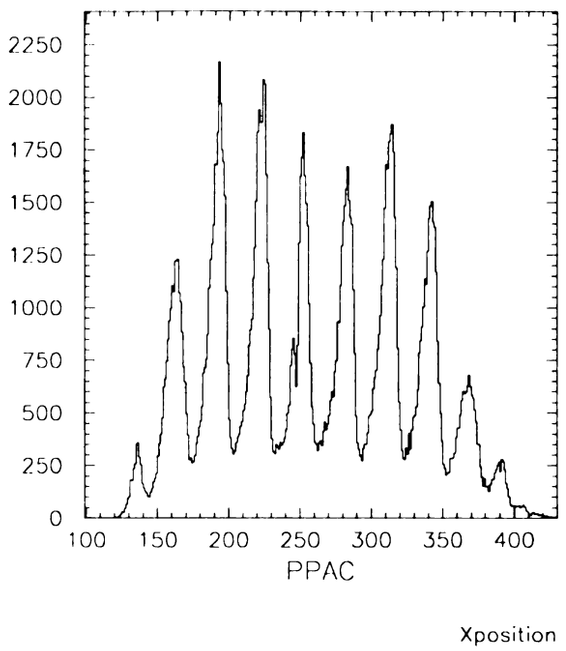

Figure 3.1: Shown are the PPAC position of Ni residue with approximate peak position. The apparent mass separation is 28 channels.

Table 3.1: Expected and observed mass peaks. Peak values for the Ca on Ni calibration run taken from 3.1.

q	M	Calc [11]	FMA
23	89	373	371
23	90	344	344
23	91	315	313
23	92	286	285
22	88	286	
23	93	257	251
22	89	256	248
23	94	228	
22	90	226	222
23	95	199	
22	91	195	193
23	96	170	
22	92	165	163
21	88	160	
23	97	141	
22	93	135	134

Table 3.2: Cross Section calculation. The FMA efficiency was calculated to be 15%.

Beam E (MeV)	Charge IQ (coul.)	ER Y (counts)	Time t (sec)	Current N_P (enA)	FMA eff. ρ (%)	Cross Sect. σ (μb)
206	352149	89392	16020	44	15	490 $\pm$ 160μb
219	88448	10202	6840	26	15	220 $\pm$ 70μb
259	44474	2917	3420	26	15	130 $\pm$ 40μb

We calculate the beam current (μ_B) from the integrated charge with a full scale (FS) of 200 enA.

$$N_P = \frac{IQ * FS}{t}[enA] \tag{3.1}$$

And with an average charge state of 10, the calculated beam current was

$$N_P = \frac{N_P[enA]}{10 * 1.6\text{E} - 19}[pA] \tag{3.2}$$

The target was ^{176}Yb with a thickness of $.81mg/cm^2$ and so $N_T = .81*6.022\text{E}20/176 = 2.77\text{E}18[cm^{-2}]$. The final cross section was then calculated to be

$$\sigma = \frac{Y}{N_P * N_T * \rho}[\mu b] \tag{3.3}$$

3.1.3 ^{48}Ca on ^{176}Yb 106 and 119 MeV

The measurements of 106 and 119 MeV show a very clean mass spectrum with only two masses surviving. Both energies produced apparently the same observed isotopes, though with a different ratio. The recorded FMA settings were identical (q_{center}=20.5, m_{center}=220) for both runs, and the results can be seen in figure 3.2. If the gain setting on the FMA calculator is matched to the charge separation (140 channels, gain 2875) the expected mass positions are those in table 3.3. Good agreement is seen between expected and observed position.

Table 3.2: Cross Section calculation. The FMA efficiency was calculated to be 15%.

Beam E (MeV)	Charge (coul)	PS (counts)	Time (sec)	Current (enA)	FMA eff.	Cross Sect. $\frac{\sigma}{\rho}$ (μb)
206	382146	85802	15020	14	15	420 ± 100μb
219	86146	19207	8540	20	15	220 ± 70μb
259	44174	2917	3450	20	15	130 ± 40μb

We calculate the beam current ($\mathcal{N}_P$) from the integrated charge with a full scale (FS) of 200 enA

$$\mathcal{N}_P = \frac{CQ \cdot FS}{t} [enA] \tag{3.1}$$

And with an average charge state of 10, the calculated beam current was

$$\mathcal{N}_P = \frac{\mathcal{N}_P[enA]}{10 \cdot 1.6E-19} [eA] \tag{3.2}$$

The target was ^{197}Au with a thickness of 81mg/cm^2 and so $\mathcal{N}_T = 81*6.022E20/197 = 2.77E18$[cm^{-2}]. The thick cross section was then calculated to be

$$\sigma = \frac{Y}{\mathcal{N}_P * \mathcal{N}_T * \rho} [\mu b] \tag{3.3}$$

3.1.3 ^{16}O on ^{197}Au 106 and 119 MeV

The measurements of 106 and 119 MeV show a very clean mass spectrum with only two masses surviving. Both energies produced apparently the same observed isotopes, though with a different ratio. The recorded FMA settings were identical (B_{dipole}=20.6, m_{quads}=220) for both runs, and the results can be seen in figure 3.2. If the gaussetting on the FMA calculator is matched to the charge separation (1-10 dianuels, gain 2870) the expected mass positions are those in table 3.3. Good agreement is seen between expected and observed position.

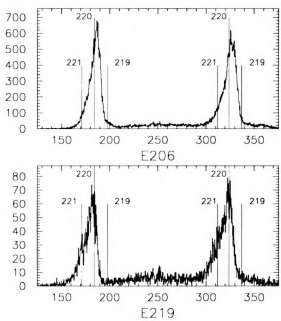

Figure 3.2: PPAC position projection of 206 and 219 MeV. The three relevant masses are labeled. Note that the 219 MeV mass labels are before assuming the correction noted in the text.

Table 3.3: 206 and 219 MeV mass distribution

Mass	Web	206MeV	219MeV
220	184	185	181
221	171	174	169
220	324	325	322
221	312	312	308

Later, when comparisons to predicted mass distributions were made, decay-times of ERs must be taken into account. The flight path of the FMA was approximately 1500 μs, with any in-target chamber or in-flight decay resulting in loss of the residue.

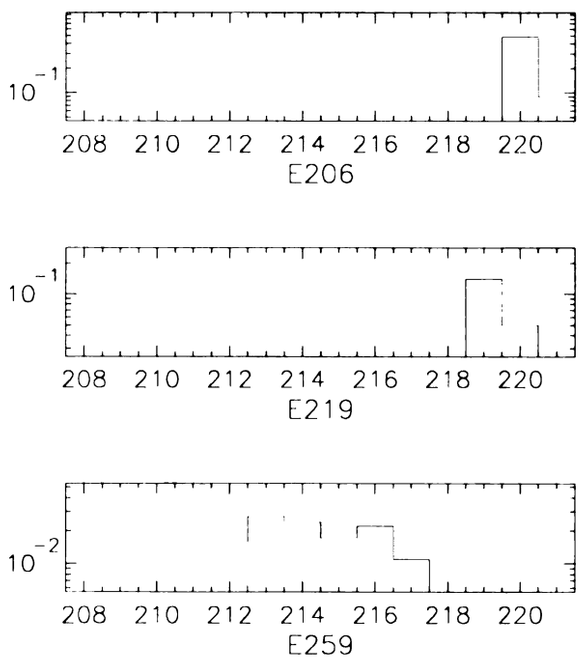

Figure 3.3: Observed isotope distribution for reactions at 206, 219 and 259 MeV. Energy 219 MeV is shifted as noted in the text.

The masses seen in the reaction at the intermediate energy (219 MeV) exhibit a significant discrepancy with previous experimental results (below) and calculations (see section 4.1). The expected residues are distinctly lower in mass than our results indicate. Previous experiments have been excecuted with a similar setup of the FMA. One such experiment, completed by Heinz [12] provides results shown in figure 3.4. The discrepancy can be reconciled by a shift of our recorded FMA settings by one mass lower. The effect on our observed masses would be to shift lower by one amu. This shift is assumed for the rest of the analysis as given. It is assumed that the mass settings for the FMA were incorrectly recorded. Several other possible causes have been ruled out. We had concern about beam-energy drift, but could not reproduce

such a great mass shift with a reasonable energy change (±5 MeV) in EvapOR. The different isotope ratios between the energies (figure 3.3) as well as distinct time-of-flight (TOF) vs energy-loss (dE) plots (figure 3.7) preclude the argument that both were run at 206MeV. A plot of the projections of figure 3.7 (seen in figure 3.5) shows that the projections of dE and TOF follow the predicted trend. The projections plotted as a function of beam energy can be seen in figure 3.6.

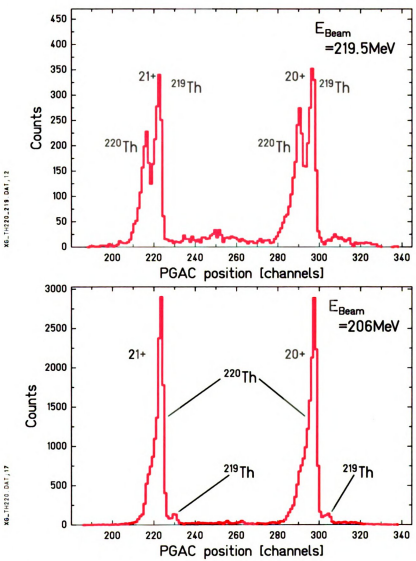

Figure 3.4: Mass distribution observed by Heinz for energies 206 and 219 MeV.

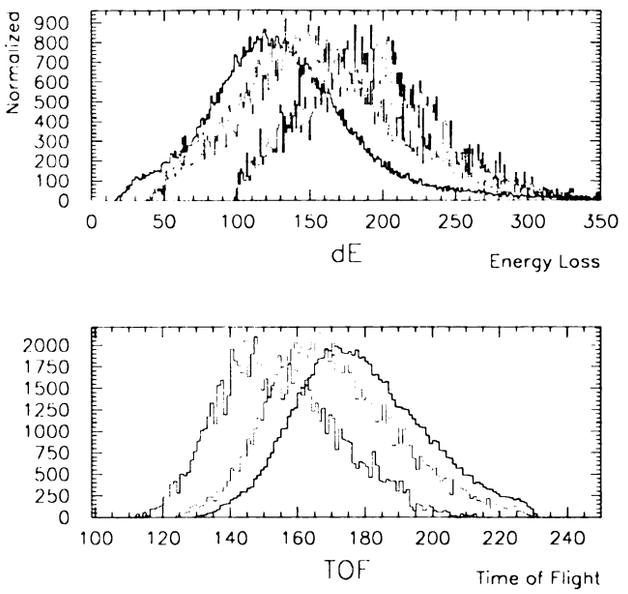

Figure 3.5: Projection of figures 3.7 and 3.9. Black is 259, red is 219 and blue is 206 MeV.

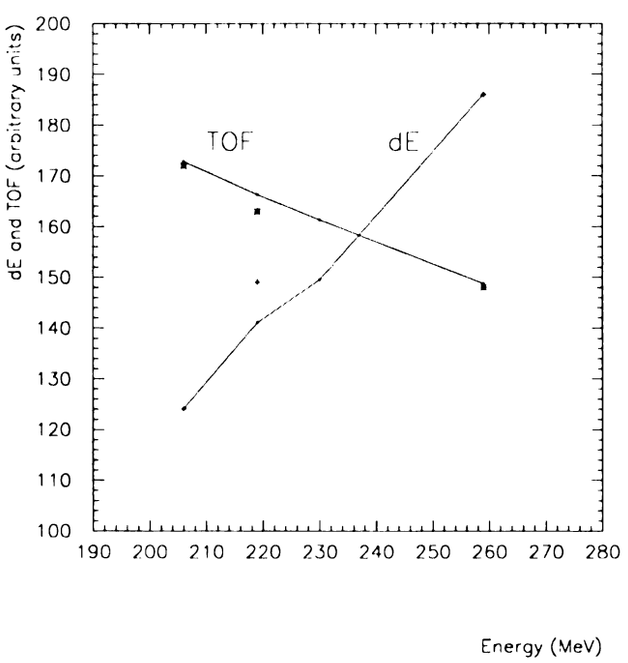

Figure 3.6: TOF and dE projection peaks plotted as a function of beam energy. Experimental points show close agreement with predicted values (line) generated by Evap. Blue: Time of Flight. Red: Energy Loss.

3.1.4 Mass Identification for ^{48}Ca on ^{176}Yb 256 MeV

Table 3.4: 256 MeV mass distribution, predicted and observed

Mass	Web	Observed
213	231	228
214	218	218
215	204	207
216	190	189
217	176	177
218	163	
219	149	
220	135	
221	121	

The mass peaks for 256 MeV were found using the 1d x position plot (figure 3.8). The position plot seems to provide acceptable peaks and a reasonable match to the calculations, the better separation on the 2d plot would indicate more accurate values. The gates were drawn on the 2d plot for this reason. A comparison of the predicted and observed mass distribution can be seen in table 3.4.

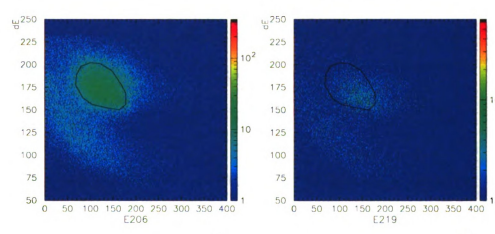

Figure 3.7: The dE-TOF plots for the 206 MeV and 219 MeV runs are distinct and different from one another. A gate for the 206 MeV is shown for reference.

3.1.4 Mass identification for ^{48}Ca on ^{176}Yb 256 MeV

Table 3.4: 256 MeV mass distribution, predicted and observed

Mass	Yield	Observed
213	231	258
214	218	218
215	204	207
216	190	189
217	176	177
218	163	
219	149	
220	135	
221	121	

The mass peaks for 256 MeV were found using the 1d x position plot (figure 3.8). The position plot seems to provide acceptable peaks and a reasonable match to the calculations, the better separation on the 2d plot would indicate more accurate values. The gates were drawn on the 2d plot for this reason. A comparison of the predicted and observed mass distribution can be seen in table 3.4.

Figure 3.7: The dE-TOF plots for the 256 MeV and 219 MeV runs are distinct and different from one another. A gate for the 256 MeV is shown for reference.

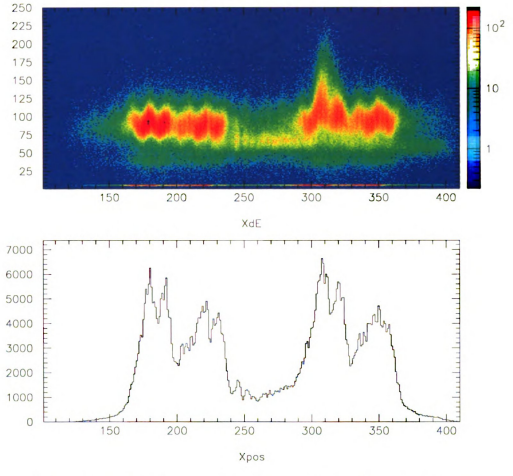

Figure 3.8: 256 MeV: Top, PPAC x vs. dE. Bottom, x projection.

3.2 Experimental GDR Spectrum

To extract the GDR parameters and compare them to predictions and past experiments we used several techniques to identify and isolate the γ-rays. Once we had an acceptable spectrum of observed γ-rays, we compared it to EvapOR calculations to establish the centroid and width of the GDR. The EvapOR spectrum was folded to take into account the detector response before the comparison was made. More on the folding process can be found in chapter 4.

3.2.1 Analysis

The γ-rays collected by the BaF_2 array were filtered in several ways. The unique ability to gate on ER events gave us the ability to exclude all γ-rays leading to fission (see chapter 1).

To ensure only ER events in the FMA, we used a time of flight vs energy-loss gate (figure 3.9) to reduce scattered beam events. The RGTac was the RF timing signal from the linac used to determine true beam events. The RGTac gate was used to further limit noise (figure 3.10). Before shower reconstruction, the γ-rays collected by the BaF_2 were filtered with a fast-slow energy gate (figure 3.11). BaF_2 has distinctly different timing characteristics for neutrons and γ-rays. Neutrons deposit a higher percentage of their energy summed in the tail of the energy peak. This results from a lower ionization rate than γ-rays. That in turn leads to more single electron and hole interactions. These single interactions comprise the majority of the tail or 'slow' signal [13].

The BaF_2 energy vs. time gate can be seen in figure 3.11. With these gates applied to the reconstructed gamma spectrum, we see a clear GDR structure around 11 MeV (see figure 3.12). We then subtracted a γ-ray spectrum with the BaF_2 time gate shifted. This subtraction accounted for the random RF bursts. The subtracted

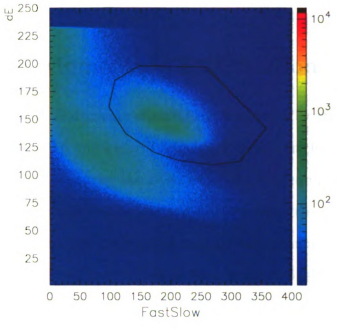

Figure 3.9: TOF vs dE with evaporation residue gate used to reduce scattered beam.

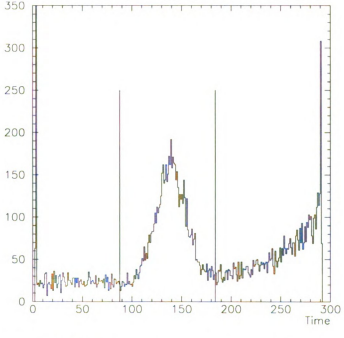

Figure 3.10: RGTac used to gate on true beam events.

gamma spectrum can be seen in figure 3.13.

3.3 Angular Momentum Distribution

The angular momentum and energy distribution measured by the BGO array was gated on the ER in the FMA and a multiplicity greater than one in the BGOs (to limit dead time). Unlike the BaF_2 array, the BGO array did not require a time-dependent calibration. The array proved stable over the two day run-time. However, an initial calibration was done before the start of the angular momentum measurements. The calibrated energy multiplicity spectra can be seen in figure 3.14 and the projections can be seen in figure 3.15.

These projections show very little peak shift between energies. Any shift is further obfuscated by the threshold impinging on the peak. However, the slope clearly becomes more shallow with increasing energy.

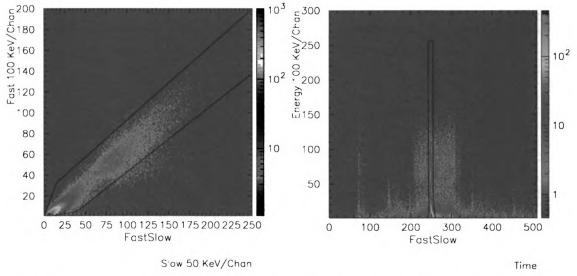

Figure 3.11: Left: Fast-slow energy gate used to reduce neutron collection. Neutron contamination can be seen below the gate. Right: BaF_2 energy vs. time gate.

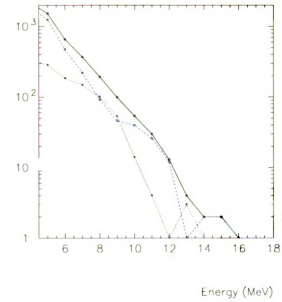

Figure 3.12: The random gamma spectrum (dotted) is subtracted off the full gamma spectrum (solid) that results in the final spectrum (dashed).

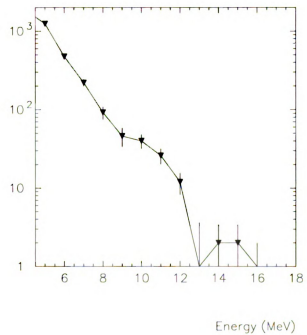

Figure 3.13: Fully gated gamma spectrum with random subtraction.

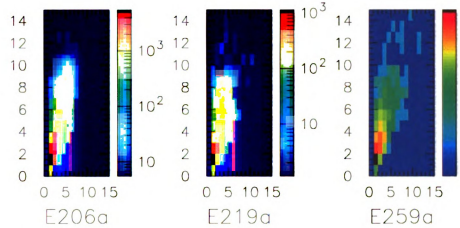

Figure 3.14: Experimental angular momentum distribution. Y-axis: Energy in MeV. X-axis: γ-ray multiplicity

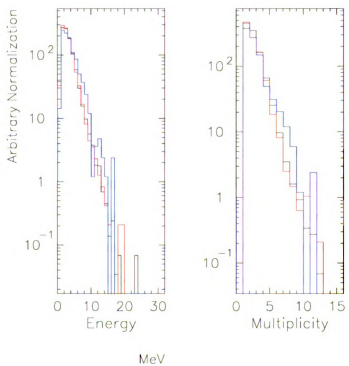

Figure 3.15: Experimental angular momentum and energy projections. Black: 206 Red: 219 Blue: 259

Chapter 4

Results

4.1 Cross Section

Figure 4.1 shows the only previous values for the cross section of this reaction. The work only considered the 4-n channel at slightly lower excitation energies. At 256 the 4-n channel becomes much less significant, accounting for the drop seen by Sahm [14].

Our simulations with the Monte-Carlo code EvapOR [15] were adjusted slightly to normalize the cross section at the lower energy. This was done by changing the fission barrier to .95 to lower the overall cross section. However, lowering it below .95 caused an acute shift to a lower mass distribution. The figure also shows the experimental 4-n channel for comparison. The EvapOR code was modified [16] to use Reisdorf [17] level density parameters. A significant improvement was made in the comparison of the mass distribution when the level density calculation was changed. A comparison of the observed and predicted mass distribution can be seen in figure 4.2. The EvapOR distribution was then adjusted to take into account lifetime considerations (particularly Ra 216-219). The flight path of the FMA was approximately 1500 ns, with any target chamber or in-flight decay resulting in loss of the residue.

Past experiments have shown a distinct underprediction of the cross sections at

Chapter 4

Results

4.1 Cross Section

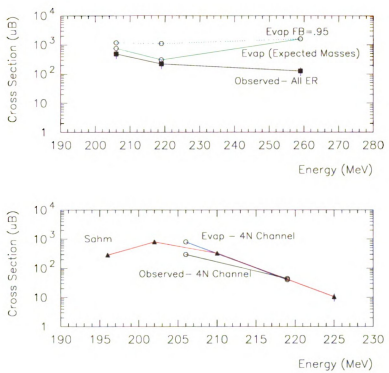

Figure 4.1: Previous experimental, predicted and observed cross sections.

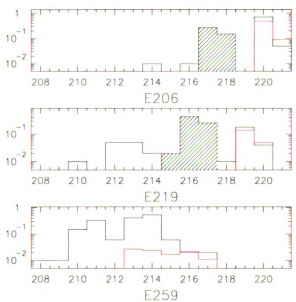

Figure 4.2: Comparison of the expected and observed yield of isotopes. Black: predicted by EvapOR. Diagonal hash: Not seen because of lifetime constraint (1500 ns). Red: Observed.

high energies by statistical models. One such experiment by Brinkmann [2] produced much higher cross sections above 110 MeV than predicted by statistical models (see figure 4.3). They were unable to achieve the saturation of cross section at higher energies with standard parameters. Even severe fission hindrance did not achieve an acceptable fit.

Our cross section measurements were an effort to explore this further. The fact that the measured cross sections were not significantly higher than the statistical model discourage the suggestion that fission dissipation is the root of the ^{16}O discrepancy. Recently, Berriman [3] has pointed to a different solution. Incomplete fusion has been shown to enhance the cross section at high energies. Figure 4.4 shows the affect of removing the incomplete fusion from the cross section measurement. Because the ^{16}O experiment was highly mass asymmetric, it is likely that there was a significant effect from incomplete fusion. The lack of extreme mass asymmetry and excess cross section also supports this explanation.

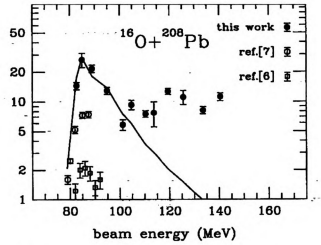

Figure 4.3: Enhanced cross section at higher energies previously observed by Brinkman (figure reprinted from [2])

4.2 EvapOR Predictions of the GDR

The GDR parameters have traditionally been extracted from the experimental spectrum through a comparison with theoretical computational models. The models are iteratively adjusted to match the experimental data. In the past, programs such as MorschFit [18] have been used in conjunction with statistical codes to automate the process. However, current statistical models are unable to provide us with ER gated gamma-spectrum, so we were forced to use a full Monte-Carlo simulation (EvapOR). The use of EvapOR made an automated search for the parameters untenable. Instead, we started our calculations with results from earlier work by Dioszegi [19,20] and Butsch [21].

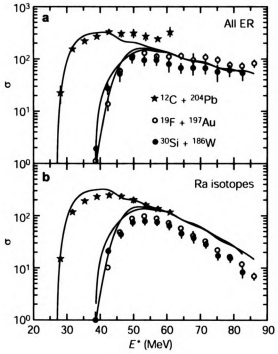

Figure 4.4: (a) All ER (b) Incomplete fusion ER removed. (figure reprinted [3])

4.2.1 Previous Experimental Results

Previous studies of ^{224}Th have suggested values of the two component GDR seen in table 4.1. The results from Butsch were fission gated ^{16}O+^{208}Pb at an excitation energy of 82 MeV. Their data indicated a highly deformed prolate state that results in a greater splitting than was seen in our data. Dioszegi's 2000 data supports an oblate CN and prolate SSC as shown. Due to the extreemly low statistics, our measurement does not confidently resolve the CN shape. However, the data seems to fit best to the previously observed oblate shape.

Table 4.1: Previous Experimental GDR Parameters for ^{224}Th in units of MeV

	E_1	Γ_1	E_2	Γ_2
Dioszegi (oblate) [19]	11.2	4.5	12.2	5.3
Dioszegi (prolate) [19]	9.7	4.5	12.4	7.3
Butsch [21]	9.8	2.5	15.5	5.0

4.2.2 EvapOR GDR Spectrum and Detector Response

Detector response was taken into account by folding the Evap spectrum with a simulated detector response. A Monte-Carlo Geant simulation (figure 4.5) was performed to construct this response function. The simulation used the individual detector energies (figure 4.6) in the same shower reconstruction code used in the experimental analysis. The folded EvapOR γ-ray spectrum can be seen in figure 4.7. A subtle effect can be seen in the folded spectrum, primarily a shift to lower energy. There is also a slight filling of the local minimum around 9 MeV.

4.2.3 Theoretical Comparison of GDR Parameters

The EvapOR calculation was run for eighty million events, 99.644% of which fissioned immediately. The remaining 284,800 events were folded and scaled to match the raw

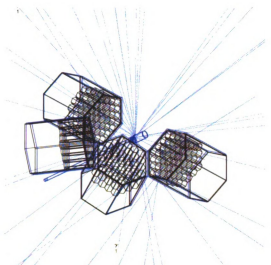

Figure 4.5: Geant simulation with emission of 4 MeV γ-rays.

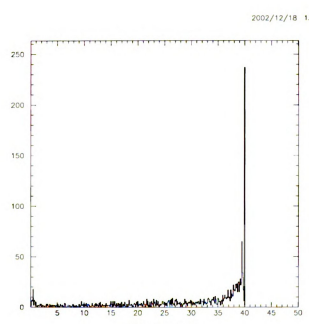

Figure 4.6: A sample spectrum from a BAF detector resulting from a 4 MeV γ-ray. This shows the typical shift lowering the energy due to detector response.

count of evaporation residue from the experiment. This affect can be seen in figure 4.7. During the four day run, 763,240 ERs were deposited in the FMA. A final comparison of the predicted GDR with the observed spectrum is seen in figure 4.8. Figure 4.9 shows EvapOR run with the other observed values as well. Overall agreement is good, though there is some overprediction of the GDR strength in all predicted spetra.

4.3 EvapOR h-k Simulations

The EvapOR monte-carlo code was used to predict the angular momentum and energy population for all three energies. The raw predictions (without detector response folding) can be seen in figure 4.10 and the projections in figure 4.11.

The EvapOR events were folded in a similar manner to the GDR spectrum to account for detector response. However, the energy response was not folded into the calculation, only the multiplicity response. A two dimensional multiplicity response

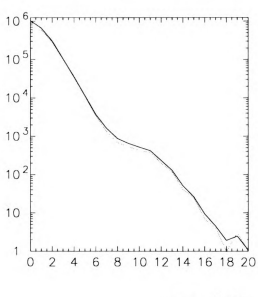

Figure 4.7: Folding in the detector response has a subtle affect, shifting the spectrum slightly lower and filling in the region around 9 MeV. (Solid Folded) The folded spectrum is arbitrarily scaled to the original at 4 MeV.

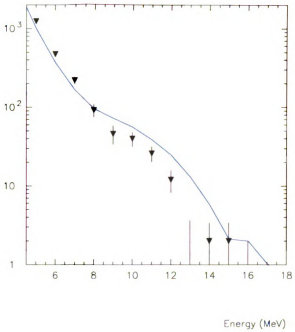

Figure 4.8: The experimental gamma spectrum compared to the EvapOR calculations using Dioszegi's oblate GDR parameters.

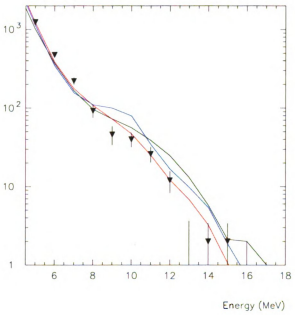

Figure 4.9: Evap simulations based on previous experimental GDR parameters. Note the energy scale is adjusted to best display both plots.

function was created using GEANT. The simulation was performed with 1 MeV γ-rays which was the approximate average energy observed.

The predictions (as seen in figure 4.12) shows a monotonic trend between energy and h-k distribution. The projections (figure 4.13) show both temperature and angular momentum increasing from 206 to 219 to 259 MeV. A comparison between the experimental and Monte-Carlo results can be seen in figure 4.14. Though the trend is less evident in the experimental plots, good agreement is seen between the EvapOR calculations and data.

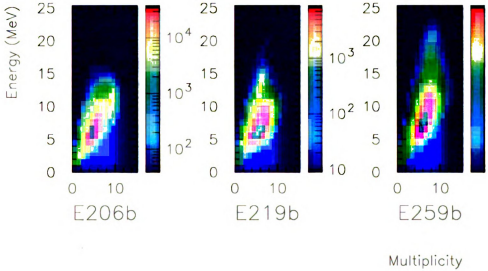

Figure 4.10: EvapOR angular momentum distribution prior to folding.

The good agreement in the folded and projected energy and multiplicity indicates that the EvapOR calculations are appropriate in this case. Now plotting the entry angular momentum distribution we see that the ER clearly emanates from the expected low angular-momentum region. There is a slight underprediction of the higher angular momentum region around a multiplicity of 10.

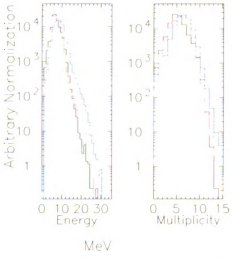

Figure 4.11: EvapOR angular momentum and energy projections prior to folding. Black: 206, Red: 219, Blue: 259.

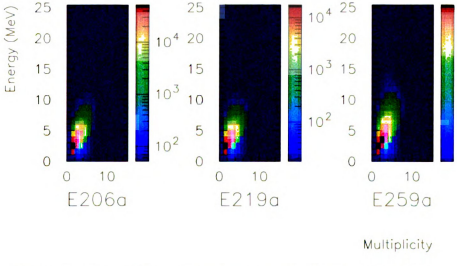

Figure 4.12: EvapOR angular momentum distribution after folding.

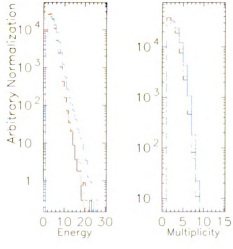

Figure 4.13: EvapOR angular momentum and energy projections after folding. Black: 206, Red: 219, Blue: 259 MeV.

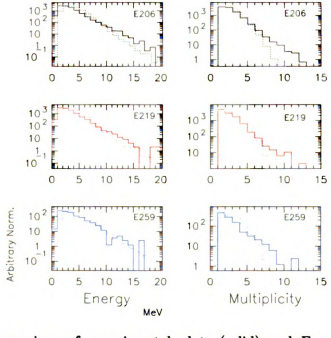

Figure 4.14: Comparison of experimental plots (solid) and EvapOR projections (dashed).

Chapter 5

Conclusion

Using the reaction ^{48}Ca on ^{176}Yb to study highly excited ^{224}Th, we successfully measured the cross section, GDR strength function and angular momentum distribution in coincidence with evaporation residues. The reaction provided a unique challenge stemming from extremely high fission probability. This experiment was the first observation of GDR in such a heavy system without fission γ-rays.

The cross section and mass distribution of the system matched standard statistical codes with minimal adjustments to the parameters. There was a slight deficiency of the lower masses at the highest energy (256 MeV) when compared to the predicted distribution from EvapOR. The 4-n cross section was found to closely match previous experimental results. There is no prior experimental measurement of the other decay channels, but our total cross section remained below the predicted total cross section. No evidence of a cross section enhancement at the highest excitation energy confirms the results by Berriman *et. al.*

Even with extremely low statistics, the GDR was measured successfully at the highest energy. The GDR function for energy 256 MeV was found to fit standard parameters: E_1=11.2 MeV, Γ_1=4.5 MeV E_2=12.2 MeV, Γ_1=5.3 MeV. The data supports a smaller deformation than the previously observed pre-fission GDR. No

evidence of fission hindrance was expected or observed in the GDR. A mild overprediction by Evap of the GDR strength was noted.

Predicted angular momentum distributions fit well to the measurements made at all three energies. As expected, there is no evidence of evaporation residue cascading from beyond the fission barrier. There is however, a slight excess of the ER coming from high angular momentum (around 10 $\hbar$). This absence from Evap's yield hints at hindrance. The Monte-Carlo (Evap) code does not incorporate the affect of hindrance. The statistical (CASCADE) code does have methods to incorporate hindrance, but inclusion does not significantly better the fit.

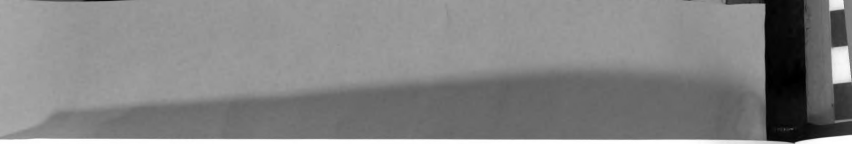

Appendix A

Distributive Computing with EvapOR

CASCADE's inherent limitations required the use of a rigorous monte-carlo to perform fission traceback. EvapOR, as a well tested evaporation code was an obvious solution. However, the increase in required computing power ruled out previous fitting techniques (such as MorschFit [18]). Due to the low evaporation residue cross section (approximately 1%), reasonable statistics for the high energy γ-rays required 10–20 hours of CPU time. This CPU time would easily turn into days of real time. An attempt to tweak any number of the input parameters for the reaction quickly turned into an untenable problem with computational limitations. The SETI [22] program, and other well know distributive computing systems spawned the idea to use the desktop PCs in the lab to perform the EvapOR cascades in parallel.

A.1 Structure

To build the distributive system, an attempt was made to make it as flexible as possible. The goal was to develop a harness which would run on the client computer

and execute whatever program that was sent. The client program in this case accepted a work unit like that in table A.1. The returned data was then combined with other data sets. The client computer merely needed a program to run in the background, accept the work unit, run the application and return the dataset.

Table A.1: Sample work unit sent to client. Fields are separated by an astrik (*). The first file is the name of the batch file to be sent and run.

* shaw winEvap.exe shaw.inp mass.dat	* shaw.out shaw.pax *
files to be sent	files to return

The host computer was required to cue work units, cue clients, serve application files and accept data sets. To do this, Java provided the most flexible and platform independent form. The system consists of three programs, one for the client and two for the host.

A.1.1 Client

The client runs the program **batter**. The program implements readily available routines to control network communication. When started, the program automatically starts listening on a specified port for a work unit. It will accept that work unit only if it matches the IP address of the host computer (hard-coded into the client software). To enhance security, the work unit must match the format exactly, and the client will only retrieve the application from the known host. The client then attaches to the host using standard FTP protocol to download any of the necessary files. After a successful download, the application is executed. The resulting data files are uploaded in the same manner. For security, the host FTP server only serves from the server **runfiles/** directory and accepts uploads to the root directory.

A.1.2 Host

The host runs the program `coach` that has two main threads. The first listens and cues requests from clients for jobs. The list is a FIFO list which holds the IP address of the clients. The second maintains a list of work units from the file jobs.txt. If both lists are not empty, a work unit will be sent to the client. The host must also maintain an active FTP server with the correct directory structure and user-names. If the FTP server is not active, the clients will hang when they attempt to log in.

A.2 Performance

Though most of the desktop PCsare considerably slower than the UNIX or Linux machines in the lab, the distributive computing was considerably faster. Average time-scales were on the order of 3-6 hours for 40 million events. That is compared to roughly 2 million events for the comparable time on the SpiceRack and 1 million events on the Unix machines. A significant gain was made in the robustness as well. No longer was the time dependent upon shared resources and possible computer down-time. Even with 10% of the clients not responding, the performance was not significantly affected. The relatively infinite scalability of the client force means that any minor loss due to down-time can be recouped by scaling the workforce. Very few negative effects were observed. If the host crashed, there was no adverse affect, but if the FTP server crashed, it would hang the clients. The clients are also impossible to kill or restart remotely. Once a work unit is started, the client will not accept new units.

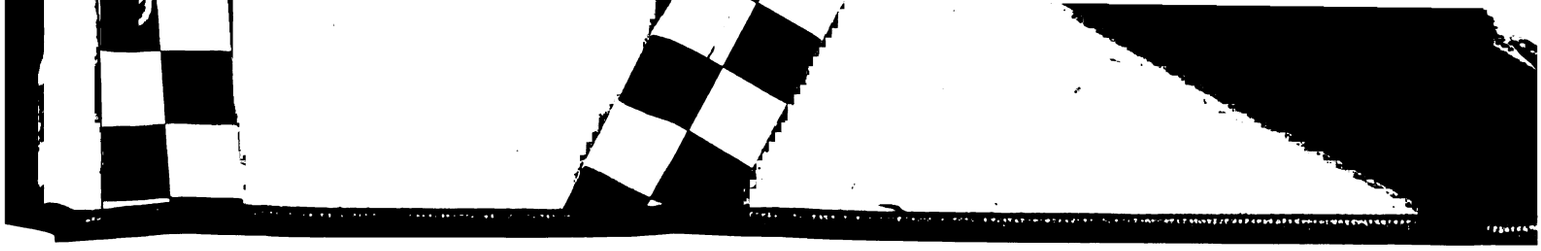

Bibliography

[1] Michael Thoennessen and J.R. Beene. Nuclear dissipation and the feeding of superdeformed bands. *Phys. Rev. C*, 45:873–875, February 1992.

[2] K.-T. Brinkmann, A.L. Caraley, B.J. Fineman, N. Gan, J. Velkovska, and R.L. Mcgrath. Residue excitattion functions from complete fusion of ^{16}O with ^{197}Au and ^{208}Pb. *Phys. Rev. C*, 50:309–316, July 1993.

[3] A.C. Berriman, D.J. Hinde, M. Dasgupta, C.R. Morton, R.D. Butt, and J.O. Newton. Unexpected inhibition of fusion in nucleus-nucleus collisions. *Nature*, 413:144–147, September 2001.

[4] E. Rutherford. The scattering of a and b particles by matter and the structure of the atom. *Philosophical Magazine*, 21:669–688, May 1911.

[5] George F. Bertch. Vibrations of the atomic nucleus. *Scientific American*, 248:62–74, May 1983.

[6] Neils Bohr and B.R. Mottelson. *Nuclear Structure.* Benjamin, new york edition, 1969. Vol. 1.

[7] Jos van Schagen. *The angular momentum and temperature dependence of the GDR in Dy nuclei.* Vrije University, 1992. Thesis, Unpublished.

[8] Peter Paul and Michael Thoennessen. Fission time scales from giant dipole resonances. *Annu. Rev. Nucl. Part. Sci.*, 44:65–108, 1994.

[9] M. Thoennessen and J.R. Beene. Nuclear dissipation and the feeding of superdeformed bands. *Phys. Rev. C*, 45:873, 1992.

[10] T.L. Khoo. Private communication.

[11] FMA Calculator. www.phy.anl.gov/fma/index.html.

[12] Heinz and T.L. Khoo. Private communication.

[13] Leo. *Techniques for Nuclear and Particle Physics Experiments.* Springer-Verlag, 2nd edition, 1994.

[14

[13

[16

[17

[18

[19

[20

[

[14] C.-C. Sahm, H.-G. Clerc, K.-H. Schmidt, W. Reisdorf, P. Armbruster, F.P. Hessberger, and D. Vermeulen. Fusion probability of symmetric heavy, nuclear systems determined from evaporation-residue cross sections. *Nucl. Phys. A*, 441:316–343, February 1985.

[15] Jim Beene. Private communication.

[16] Paul Heckman. Private communication.

[17] W. Reisdorf. *Z Physica*, A300:227–227, 1981.

[18] Michael Thoennessen. Private communication.

[19] I. Dioszegi, N.P. Shaw, I. Mazumdar, A. Hatzikoutelis, and P. Paul. Nuclear viscosity of hot rotating ^{224}th. *Phys. Rev. C*, 61:024613–024613, January 2000.

[20] I. Dioszegi, C.P. Montoya D. J. Hofman, S. Schadmand, and P. Paul. Giant dipole resonance decay from fusion-fission and quasifission of hot thorium nuclei. *Phys. Rev. C*, 46:627–636, August 1992.

[21] R. Butsch, D.J. Hofman, C.P. Montoya, P. Paul, and M. Thoennessen. Time scales for fusion-fission and quasifission from giant dipole resonance decay. *Phys. Rev. C*, 44:1515–1527, October 1991.

[22] www.seti.org. Search for extraterrestrial intelligence.